Componentality-based wall-blocking for RANS models

By M. Emory AND G. Iaccarino

1. Motivation and objectives

Although there has been increased adoption of large-eddy simulation (LES) in academic and industrial applications, the affordability of the Reynolds-averaged Navier-Stokes (RANS) approach ensures it will continue to be one of the most popular methods for solving these complex flows (O'Sullivan *et al.* 2012). There are still many shortcomings with most common RANS closures (i.e., turbulence models), for example difficulties due to both the physical assumptions and the numerical stiffness, or the inability to reproduce turbulence near solid walls. Proper prediction of the near-wall region is critical for accurately capturing many flow characteristics of engineering interest, e.g., friction, heat transfer, or separation.

The presence of a solid wall influences turbulent flow primarily through two mechanisms. The first is through viscous effects which require that the velocity in all directions to be zero at the wall. The second mechanism, known as the blocking effect, is due to the impermeability of the solid boundary. This effect suppresses fluctuations primarily in the wall normal direction, creating highly anisotropic turbulence structures in the near-wall region (Manceau & Hanjalić 2002). The blocking effect is sensitive to the topology of the wall and is further complicated by the reflection of pressure fluctuations off the wall, which can reduce the turbulence anisotropy. This anisotropy is often not captured or only poorly represented by common turbulence models.

Incorporating the wall-blocking effect in RANS closures has been approached in several ways, the most popular of which is through empirical damping functions, essentially a correction to the eddy-viscosity, which fits the near-wall turbulence behavior to either theory or direct numerical simulation (DNS). These corrections often suffer from a lack of physical justification and poor performance in flows with complex geometry (Billard 2007).

A different approach was taken by Durbin (1991) where two additional equations are added to a standard $k-\epsilon$ model. The first is a transport equation for $\overline{v^2}$, representative of the wall-normal velocity fluctuations, a term which damps the eddy-viscosity near walls. The second is an elliptic equation which describes the generation of $\overline{v^2}$ due to pressure redistribution. While this approach has shown good results in several flows, there are numerical stiffness issues related to the coupling of the additional elliptic and transport equations.

This elliptic relaxation approach has also been adapted for complex RANS modeling frameworks. The algebraic structure based model (ASBM) introduces a blockage tensor, based on a similar parameter to $\overline{v^2}$, to include proper wall-blocking (O'Sullivan *et al.* 2012) while Durbin (1993) and Manceau & Hanjalić (2002) have extended the approach to Reynolds-stress transport models. The complexity of these RANS approaches, however, limits adoption of these models by industry.

Capturing wall-blocking effects is an important challenge at all levels of RANS model

complexity. This work focuses on developing an alternative to damping functions which introduces wall-blocking in two-equation RANS models. The approach is guided by two objectives:

(*a*) to develop a methodology to cost-effectively introduce wall-blocking effects to eddy viscosity models,

(*b*) to use an approach which is physically motivated and not an empirical fit to data. The first objective is self-explanatory; when driven by short design cycles one does not want to use a wall-blocking methodology which makes the RANS approach significantly more expensive than standard RANS models. We focus in particular on eddy viscosity models because of their prevalent use by industry; however, we will show that the proposed methodology can be used in conjunction with other RANS modeling frameworks as well. The second objective is designed to differentiate this work from the damping function approach. Damping functions are limited by their calibration to validation data; in an arbitrary flow they are credible only if sufficient calibration data are available.

In Section 2 we present a new framework to introduce wall-blocking in RANS turbulence models. In this section we also describe a specific implementation and perform an a priori analysis of how one can expect this wall-blocking to influence a basic flow. In Section 3 the proposed wall-blocking framework is applied to three test cases: developed turbulent channel flow, transonic flow over a bump geometry, and the flow past a wing-body junction.

2. Wall-blocking methodology

2.1. *Theoretical approach*

2.1.1. *The barycentric map*

It is well known that even for simple flows RANS eddy-viscosity models poorly reproduce turbulence anisotropy, defined as

$$a_{ij} = \frac{R_{ij}}{2k} - \frac{\delta_{ij}}{3}\,, \tag{2.1}$$

where $R_{ij} = \overline{u_i' u_j'}$ is the Reynolds stress and $k = R_{nn}/2$ the turbulence kinetic energy. To visualize this discrepancy we leverage the barycentric map of Banerjee *et al.* (2007), a non-linear anisotropy invariant map. This mapping relies on the observation that any state of turbulence anisotropy a_{ij} is a convex combination of the three limiting states of one-component (1C), axisymmetric two-component (2C), and isotropic (3C) turbulence. These states classify turbulence based on the relative magnitudes of the Reynolds stress eigenvalues φ_i, i.e., the magnitudes of the principal normal stresses. We first describe these states and their manifestation within the barycentric map† which is shown in Figure 1:

(*a*) one-component: describes turbulence where only a single φ_i is non-zero, indicating that turbulent fluctuations only exist along one direction. This state is also referred to as rod-like' or cigar-shaped turbulence, a visual description which evokes the one-dimensional nature of this state. This state is the bottom right corner of the barycentric map $\mathbf{x}_{1C} = (1, 0)$;

(*b*) axisymmetric two-component: describes turbulence where two φ_i are non-zero and of equal magnitude, also referred to as pancake-like turbulence. This state is the lower

† Although the location of these points can be chosen arbitrarily, we follow the equilateral triangle convention described by Banerjee *et al.* (2007).

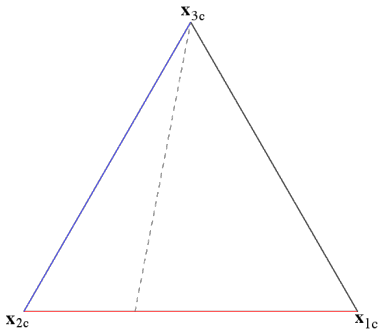

FIGURE 1. Barycentric map of Banerjee *et al.* (2007), highlighting the two-component limit (bottom boundary) and the plane strain limit (dashed line).

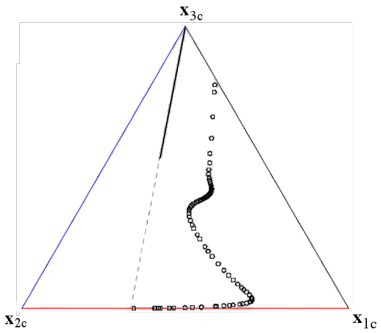

FIGURE 2. Channel flow ($\mathrm{Re}_\tau = 2003$) profiles of turbulence anisotropy plotted within the barycentric map. Results from direct numerical simulation (Hoyas & Jimenez 2006) are represented by circles; from RANS, the SST $k-\omega$ model of Menter (1994), by a solid line.

left corner of the barycentric map $\mathbf{x}_{2C} = (0, 0)$. Note that this is a limiting state of the more general two-component turbulence (the lower boundary of the barycentric map), defined where the two non-zero φ_i are not necessarily of equal magnitude;

(c) isotropic: describes turbulence where all three φ_i are non-zero and of equal magnitude, also referred to as spherical turbulence. This state is the top corner of the barycentric map $\mathbf{x}_{3C} = (0.5, \sqrt{3}/2)$. This is a limiting state of the more general three-component turbulence, defined when there are three non-zero φ_i, i.e., anywhere within the boundaries of the triangle.

A final state worth mentioning is plane strain turbulence, defined when at least one $\varphi_i/2k = 1/3$ (or equivalently at least one anisotropy eigenvalue equal to zero). The turbulence along the principal axis corresponding to a $\varphi_i/2k = 1/3$ eigenvalue is due only to isotropic stress. This implies that the turbulence is statistically stationary in this direction, and thus anisotropy only influences the solution in the plane perpendicular to this direction.

For an arbitrary state of turbulence anisotropy, the location within the map (x_B, y_B) is defined as

$$x_B = x_{1C}C_{1C} + x_{2C}C_{2C} + x_{3C}C_{3C} = C_{1c} + 0.5C_{3C}\,, \tag{2.2a}$$

$$y_B = y_{1C}C_{1C} + y_{2C}C_{2C} + y_{3C}C_{3C} = \sqrt{3}/2C_{3C}\,, \tag{2.2b}$$

where the convex coefficients are linear functions of the anisotropy eigenvalues λ_i

$$C_{1C} = \lambda_1 - \lambda_2\,, \tag{2.3a}$$

$$C_{2C} = 2\,(\lambda_2 - \lambda_3)\,, \tag{2.3b}$$

$$C_{3C} = 3\lambda_3 + 1\,. \tag{2.3c}$$

2.1.2. *RANS prediction of anisotropy*

We illustrate the poor anisotropy representation of an eddy-viscosity model by comparing barycentric map profiles from DNS (Hoyas & Jimenez 2006) and RANS (using the SST $k-\omega$) for fully developed channel flow, shown in Figure 2. The DNS trajectory

within the map† starts near the isotropic corner (at $y/h = 1$) and snakes towards the two-component limit ($y/h = 0$) as the wall is approached. Importantly, the trajectory bends first towards the 1C corner, then towards the 2C corner for points very close to the wall. As y/h decreases, the wall-normal velocity fluctuations are suppressed and the fluctuations parallel to the wall dominate. Because the flow has a predominant direction ($\bar{u}_x \gg \bar{u}_y$), the wall-parallel fluctuations are not of equal magnitude, thus inducing the bend towards 1C. Very close to the wall, however, viscous effects damp the velocity in all directions such that the wall-parallel fluctuations are of similar magnitude, hence the profiles trend towards the 2C corner.

In stark contrast is the perfectly linear trajectory of the RANS model, which simply moves along the plane strain limit. Hidden by this particular visualization technique is the fact that the RANS model predicts 3C turbulence at both $y/h = 1$ and 0. In the RANS context‡ the flow is statistically stationary in the spanwise dimension, causing the observed plane strain behavior. A more detailed discussion of the observed RANS behavior can be found in Emory (2014, Chapter 3).

2.2. *Implementation*

We leverage the barycentric map and the observed DNS trajectory to develop a new wall-blocking approach. Working within the context of the barycentric map, for any fluid element deemed near-wall we perturb the barycentric location towards the two-component limit (bottom of the map). While Figure 2 indicates a trajectory towards first 1C then 2C is appropriate, we cannot assume the same trajectory in an arbitrary flow configuration with complex geometry. With so little knowledge about the flow, we conservatively assume that the anisotropy becomes more two-component (not necessarily 2C) as the wall is approached. We refer to this approach as componentality-based wall-blocking.

Using an arbitrarily selected RANS model, referred to hereafter as the baseline model, there are two additional computational steps required by this approach. From the perspective of a single control volume (c.v.) they are: (a) to determine whether the current c.v. is close enough to a wall boundary to be considered near-wall, and (b) if the c.v. is near-wall, to perturb the barycentric map location towards the two-component limit. The first step is fairly straightforward depending on the selected baseline model, since many already include computation of wall distance in their formulation. A raw measure of distance is not particularly informative; a more useful indicator would convey distance in terms of the local boundary layer thickness.

Whatever metric is used, its purpose is to determine whether anisotropy within the current c.v. should be perturbed. In this sense the metric is marking cells for additional manipulation, similar to the marker concept proposed by Gorlé *et al.* (2014) and Emory *et al.* (2013). To perform well, the marker, generically represented by χ, should $\in [0, 1]$ where a magnitude of zero implies the current c.v. is not near-wall while a magnitude of one is near-wall.

The second step requires a modification of the Reynolds stress anisotropy close to the wall, which is better understood graphically by plotting the baseline Reynolds stress in the barycentric map. We define this initial location¶ as $\mathbf{x}_{B,0} = (x_{B,0}, y_{B,0})$. We move this location towards the two-component limit (down in the map) by scaling the y-coordinate

† This result and other DNS databases have motivated several wall-blocking approaches, all of which attempt to model the observed trajectory.

‡ Solved using a 2D mesh with symmetry boundary conditions in the spanwise direction.

¶ Note that this location will be different for each c.v.

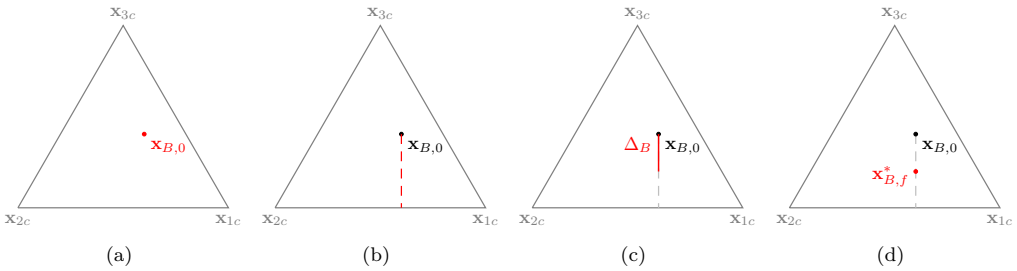

FIGURE 3. Anisotropy eigenvalue perturbation methodology. First the baseline anisotropy $\mathbf{x}_{B,0}$ is computed (a). A line is drawn towards the two-component boundary (b), and a distance Δ_B is traversed along this line (c). The resulting location $\mathbf{x}_{B,f}$ corresponds to a new set of eigenvalues (d) which are used to reconstruct the Reynolds stress.

such that

$$y_{B,f} = (1 - \chi\Delta_B)\, y_{B,0}\,, \tag{2.4}$$

where $\Delta_B \in [0, 1]$ is a free parameter (constant for all c.v.s throughout the simulation) related to the strength of perturbation. When the current c.v. is far from walls ($\chi = 0$), the barycentric map location is unchanged. Conversely, when the c.v. is considered near-wall ($\chi \approx 1$), the distance translated within the barycentric map is linearly related to Δ_B. This procedure is described visually in Figure 3.

To understand how the perturbed barycentric map location corresponds to the Reynolds stress, we represent the baseline Reynolds stress as

$$R_{ij} = 2k\left(\frac{1}{3}\delta_{ij} + v_{in}\Lambda_{nl}v_{jl}\right)\,, \tag{2.5}$$

where we have decomposed the stress into turbulence kinetic energy k and the turbulence anisotropy eigenvalues Λ_{nl} and eigenvectors v_{in}†. The new location $(x_{B,0}, y_{B,f})$ uniquely maps to a new set of anisotropy eigenvalues Λ^*, which are used to construct the perturbed Reynolds stress

$$R^*_{ij} = 2k\left(\frac{1}{3}\delta_{ij} + v_{in}\Lambda^*_{nl}v_{jl}\right)\,. \tag{2.6}$$

The perturbed Reynolds stress field R^*_{ij} is used in the RANS momentum equations instead of R_{ij}. The effect of the perturbation on the solution depends on the choice of Δ_B and the spatial distribution of χ. For numerical stability it is important that the spatial distribution of R^*_{ij}, and relatedly χ, be smooth. In future work the value of Δ_B should be calibrated, however in this work we do not attempt to select an optimal value.

The results presented in this brief all use the RANS solver `JOE`, which performs parallel calculations on a collocated unstructured mesh using a finite volume formulation and implicit time-integration. This code has been developed at the Center for Turbulence Research, and is described in detail in Pečnik *et al.* (2012) and Emory (2014, Appendix A).

† Λ_{nl} is the traceless diagonal matrix of anisotropy eigenvalues λ_l. The tensors v and Λ are ordered such that $\lambda_1 \geq \lambda_2 \geq \lambda_3$; all subsequent references to these tensors assume this ordering has taken place.

2.3. *A priori analysis*

We perform an analysis of the proposed wall-blocking perturbations for a single c.v., assuming that locally $\chi = 1$. We represent the new y-coordinate within the barycentric map as $y_{B,f} = (1 - \Delta_B) y_{B,0}$. Recall that $y_{1C} = y_{2C} = 0$, thus from Eq. (2.2) any change in y_B is linearly related to the coefficient C_{3C}. Combined with the requirement that $\sum C_{iC} = 1$, we can construct a set of perturbed coefficients

$$C^*_{1C} = C_{1C} + \frac{\Delta_B}{2} C_{3C} \,, \tag{2.7a}$$

$$C^*_{2C} = C_{2C} + \frac{\Delta_B}{2} C_{3C} \,, \tag{2.7b}$$

$$C^*_{3C} = C_{3C} - \Delta_B C_{3C} \,. \tag{2.7c}$$

that correspond to the new location $(x_{B,0}, y_{B,f})$ in the barycentric map. Not surprisingly, the change in magnitude for all three coefficients is determined by the initial value of C_{3C}, a reflection of the perturbation strategy which only modifies y_B. Incorporating Eqs. (2.3)-(2.7) we represent the change in magnitude of the anisotropy eigenvalues λ_i after perturbation as

$$\lambda^*_1 = \lambda_1 + \frac{\Delta_B}{12} \left(15\lambda_3 + 5\right) \,, \tag{2.8a}$$

$$\lambda^*_2 = \lambda_2 + \frac{\Delta_B}{12} \left(-3\lambda_3 - 1\right) \,, \tag{2.8b}$$

$$\lambda^*_3 = \lambda_3 + \frac{\Delta_B}{12} \left(-12\lambda_3 - 4\right) \,. \tag{2.8c}$$

Note that (a) the condition that $\sum \lambda_l = 0$ is maintained, (b) for $\Delta_B = 0$ the baseline eigenvalues are recovered, and (c) the change in magnitude is uniquely related to the baseline λ_3. Thus for $\lambda_3 = -1/3$ (along the two-component boundary) there is no change in the eigenvalue magnitudes. This ensures realizability (the boundaries of the barycentric map are not exceeded). For $-1/3 < \lambda_3 \leq 0$ the magnitude of λ_1 always increases, while λ_2 and λ_3 decrease. Importantly, λ_3 decreases much more rapidly relative to λ_2, promoting two-component behavior ($\lambda_1 > \lambda_2 \gg \lambda_3$).

Let us apply this perturbation to an example of a problem by considering a locally plane shear flow where $\partial_2 \widetilde{u}_1 = S$ is the only non-zero component of the velocity gradient tensor. An eddy-viscosity RANS model would generate the anisotropy tensor $a_{12} = a_{21} = -\nu_t S/k$ with all other components equal to zero. The eigenvectors for this case would be directed $\pm 45^\circ$ from the horizontal axis, and along the span-wise direction.

If a more general (non-eddy-viscosity model) is used, then we can only say that $a_{13} = a_{23} = a_{31} = a_{32} = 0$. For this case it is easy to show that $v_{i2} = (0, 0, 1)^T$ is still an eigenvector, and that the remaining two eigenvectors, associated with the largest and smallest eigenvalues, respectively, are $v_{i1} = (\cos\theta, -\sin\theta, 0)^T$ and $v_{i3} = (\sin\theta, \cos\theta, 0)^T$, where θ is an angle from the horizontal axis.

For a plane shear flow, only the R_{12} component of the Reynolds stress has a direct effect on the mean momentum equation. From Eq. (2.6) we know

$$a_{12} = (\lambda_3 - \lambda_1) \sin(2\theta)/2 \,, \tag{2.9}$$

and by substituting the eigenvalues from Eq. (2.8), we can represent the perturbed anisotropy as

$$a^*_{12} = a_{12} - \frac{\sin(2\theta)}{2} \frac{\Delta_B}{4} (9\lambda_3 + 3) \,. \tag{2.10}$$

For $-1/3 < \lambda_3 \leq 0$ the Δa_{12} will be negative, thus increasing the magnitude $|a_{12}|$ and increasing the influence of the turbulent stress locally within the c.v., demonstrating that the perturbation strategy promotes anisotropy in this flow.

2.4. *The DI:TAP model*

We present results using the shear-stress transport (SST) k–ω model of Menter (1994) as the baseline. One of the most popular two-equation models in industry, the SST leverages the desirable behavior of (a) the standard $k-\omega$ model in the near-wall region and (b) the $k-\varepsilon$ model in the freestream. This combination allows for a turbulence model which can be applied through the viscous sublayer but does not suffer from boundary condition sensitivity, a known deficiency of the standard $k-\omega$. A blending function F_1 is defined so that $k-\omega$ is applied near walls ($F_1 = 1$) and $k-\varepsilon$ is used in the free-stream ($F_1 = 0$).

This description of F_1 is identical to the ideal near-wall marker χ described in Section 2.2. Because the SST model has been used widely in a variety of applications, we do not validate F_1 in terms of its ability to properly identify near-wall regions. An additional benefit to selecting the SST model is that no additional computational cost is incurred for computing the marker $\chi = F_1$. A detailed description of the eigenvalue perturbation implementation within `JOE` is provided in Emory (2014, Appendix A).

We call the combination of the baseline model and the proposed wall-blocking methodology the DI:TAP model. DI is shorthand for decreased isotropy, describing the direction of perturbation (moving down in the map is equivalent to moving away from $\mathbf{x}_{3C}$). TAP is shorthand for turbulence anisotropy perturbation, describing the implementation approach.

3. Results

Results are presented for three cases: developed channel flow, transonic separated flow, and the complex 3D flow around a wing-body junction. For the sake of brevity, the numerical setup (e.g., grid resolution, solver settings) and other details regarding the simulations will not be described. In this work we focus on how the solution is influenced by the wall-blocking methodology.

For all cases we will compare experimental data or high fidelity simulation to the baseline solution and results from DI:TAP. To understand the sensitivity of the solution to the free parameter Δ_B, we run four simulations (for each case) of DI:TAP where $\Delta_B = \{0.25, 0.50, 0.75, 1.00\}$ using F_1 as the near-wall marker.

3.1. *Channel flow*

Turbulent channel flow describes the flow between infinite-span parallel flat plates and has been investigated frequently in the turbulence modeling community. There exists a wealth of knowledge, through both experiments and DNS, of channel flow at a variety of Reynolds numbers (Moser *et al.* 1999; Kim *et al.* 1987; Moin & Kim 1982). The availability of these data is one reason the channel is a common starting point in the development and validation of turbulence models. The primary physics in this flow is turbulent boundary layer growth. After a certain distance downstream of the channel inlet both top and bottom wall boundary layers meet. The flow downstream of this point is statistically stationary.

We simulate the channel conditions specified by the DNS of Hoyas & Jimenez (2006), a flow where $\mathrm{Re}_\tau = 2003$. For detailed information regarding the numerical and geometric

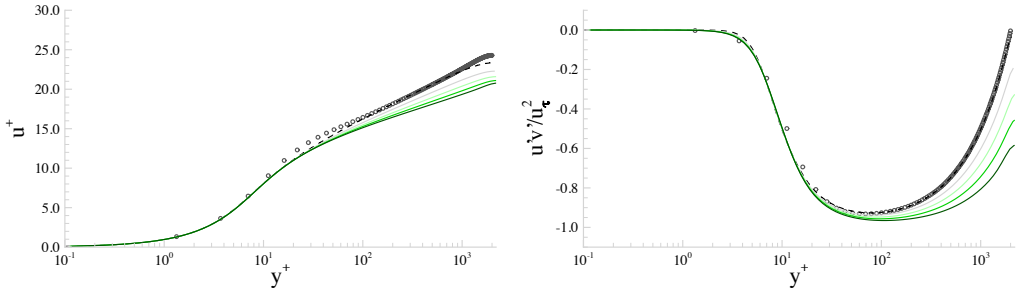

(a) (b)

FIGURE 4. $\mathrm{Re}_\tau = 2003$ channel flow profiles of (a) u^+ and (b) R_{12}/u_τ^2 versus y^+. The DI:TAP results are shown by solid lines; darker shades indicate increasing $\Delta_B = \{0.25, 0.50, 0.75, 1.00\}$. The baseline (dashed black line) and DNS (Hoyas & Jimenez 2006) results (circles) are provided for reference.

setup of this case refer to Emory (2014, Chapter 4.2). From the developed region wall-normal profiles of mean velocity $u^+ = \overline{u}/u_\tau$ and shear stress $\overline{u'v'}/u_\tau^2$ are compared with the DNS results, shown in Figure 4. The mean velocity is a typical quantity of interest in applications, while in turbulence modeling the shear stress is typically observed. This is because in 2D developed boundary layers (when $\partial/\partial x = \partial/\partial z = 0$) the only Reynolds-stress term which influences the mean momentum equation is R_{12}/u_τ^2. Note that because the flow is fully developed, the magnitude of $F_1 \approx= 1$ uniformly throughout the profile.

What is clear from both images in Figure 4 is that the DI:TAP wall-blocking does have an influence on both the mean velocity and shear stress. As the strength of the wall-blocking Δ_B increases, the deviation from the baseline becomes more dramatic. For the mean velocity the correlation to Δ_B seems asymptotic†, while for the shear stress this correlation is nearly linear. The wall-blocking has little influence on either quantity for $y^+ \leq 20$, which is appropriate because in this region viscous forces dominate and changes in turbulent stress are negligible.

In the a priori analysis in Section 2.3, we explained why the shear stress profiles increase in magnitude, i.e., become more negative, as Δ_B is increased. This correlates to reducing the magnitude of u^+ through the momentum equation, where the turbulence source term is related to $-\partial/\partial y\ R_{12}$. By increasing the magnitude of this source term, which is negative, the flow is retarded: a representation of the wall blocking the flow.

What we have not discussed yet is the fact that the wall-blocking is making the RANS prediction worse in both of these quantities. While true, this is a misleading or at least unfair conclusion to draw for two reasons:

(*a*) the baseline model has been calibrated to perform exceptionally on flows such as the turbulent channel. There is very little to improve upon for this particular flow; naturally modifications to the turbulent stress make the prediction worse.

(*b*) the baseline model, in many ways, already has a way to account for near-wall behavior. The reason the blending function F_1 exists is to use a better RANS closure near walls, so the addition of wall-blocking in this case is simply an illustration of the process rather than an attempt at improving the accuracy.

What these channel flow results have demonstrated is the DI:TAP's ability to modify the influence of turbulence when $F_1 \gg 0$ (the entire profile in this case). We observe a

† The deviation from the baseline is nearly identical for $\Delta_B = 0.75$ and 1.0.

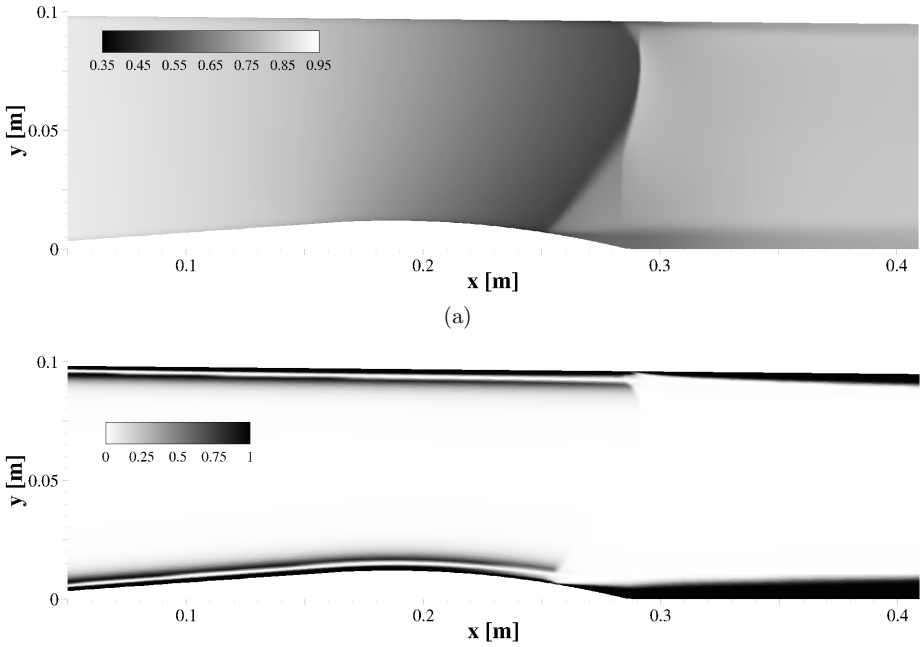

FIGURE 5. (a) Density contours for the baseline solution highlighting the presence of a lambda-shock structure downstream of the bump geometry. A large separation bubble, starting after the shock-boundary layer interaction with the oblique leg of the lambda-shock, exists along the bottom wall. (b) Contours of the the blending function F_1 demonstrate how this scalar identifies regions of the flow which are near solid boundaries.

systematic response to the magnitude of Δ_B which strongly corroborates the analysis in Section 2.3.

3.2. *Délery Case C*

We investigates the steady transonic flow over the Délery Case C bump geometry (Délery 1981), in essence a converging-diverging nozzle. Like the channel, this case is frequently used to evaluate the performance of turbulence models (Loyau *et al.* 1998; Lien & Kalitzin 2001); unlike the channel, this flow has streamline curvature, strong pressure gradients, and flow separation - physics which many RANS closures struggle to capture. The flow enters the nozzle at Mach $\simeq 0.63$ and accelerates over the bump reaching Mach $\simeq 1.36$. A normal shock emanates from the upper wall, whereas at the lower wall the shock splits into an oblique and normal leg, forming a λ-shock structure. Straining due to streamline curvature over the bump (lower wall) causes boundary layer separation (Hadjadj & Kudryatsev 2005), inducing a long thin recirculation region downstream of the shock-boundary layer interaction (SBLI). The geometry and shock structure are depicted by density contours from the baseline solution in Figure 5(a).

We simulate the conditions investigated experimentally by Délery (1981). For detailed information regarding the numerical and geometric setup of this case refer to Emory (2014, Chapter 4.4). In this flow the marker F_1 varies spatially, and contours from the baseline solution are shown in Figure 5(b). An interesting feature upstream of the SBLI is an apparent double layer, a zone within the near-wall region where F_1 briefly becomes

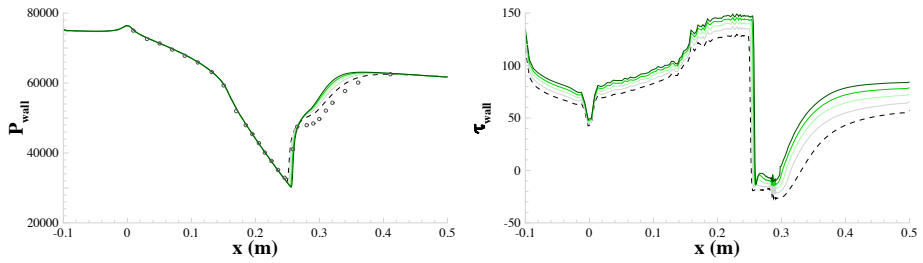

(a) (b)

FIGURE 6. Profiles of (a) wall pressure and (b) shear stress from the bottom wall. The DI:TAP results are shown by solid lines; darker shades indicate increasing $\Delta_B = \{0.25, 0.50, 0.75, 1.00\}$. The baseline (dashed black line) and experimental pressure results (circles) from Hadjadj & Kudryatsev (2005) are provided for reference.

zero. In the separated flow downstream of the SBLI, this double layer does not persist; a continuous single layer of $F_1 = 1$ penetrates towards the channel centerline from both top and bottom walls. In general, it appears as though F_1 is reasonably effective at identifying regions of the flow adjacent to walls.

We compare profiles of wall pressure and shear stress at the bottom wall, shown in Figure 6. We are interested in how the wall-blocking influences prediction of the separation bubble adjacent to this wall; the length of the bubble is determined by the distance between the $\tau_{wall} = 0$ crossing points. It is well known that the baseline model overpredicts the length of the separation bubble by as much as 30% (Emory 2014, Chapter 4.4), due to premature boundary layer separation. Correct prediction of separation size is of interest in a variety of applications. We show both pressure and shear stress profiles to demonstrate how different quantities may be more or less sensitive to the wall-blocking.

Looking first at pressure, we see that the wall-blocking only influences the solution between $0.25 < x < 0.42$; everywhere else the profiles collapse. As Figure 5(b) shows, F_1 is active throughout the domain, so the collapse of the profiles is related to the insensitivity of the pressure distribution to the wall-blocking. The separation location moves slightly downstream with increasing Δ_B, a slight improvement over the baseline model. The pressure recovers much faster as Δ_B increases, the wrong trend relative to the experimental data.

Looking now at shear stress, there are several interesting observations: first is that the DI:TAP profiles are sensitive to Δ_B uniformly throughout the domain. As Δ_B increases the shear stress at the wall increases, an intuitive consequence of the wall impeding the flow more strongly. A second observation is that the separation bubble decreases in length as Δ_B increases. Though no experimental data are available for shear stress, the separation and reattachment locations listed in Table 1 show a marked improvement in the prediction of the separation bubble length relative to the baseline. Most of this improvement comes from an improved prediction of the reattachment location while the predicted separation is relatively stationary.

These results have shown that this wall-blocking implementation can improve the characterization of separation by the baseline model (one of its weaknesses). The introduction of anisotropy in the near-wall region has improved the baseline model iresult, which was not evident in the channel. In contrast to the channel results, the marker F_1 plays an important role in spatially restricting the anisotropy eigenvalue perturbation and has performed appropriately and robustly. A final lesson learned from Figure 6 is that dif-

Case	Δ_B	x_s/h	L_s/h
experiment		22.08	5.00
SST		21.07	6.50
DI:TAP	0.25	21.21	4.99
DI:TAP	0.50	21.35	4.22
DI:TAP	0.75	21.47	3.66
DI:TAP	1.00	21.58	3.23

TABLE 1. Comparison of separation location x_s and separation bubble length L_s (difference between separation and reattachment locations) between experiment (Hadjadj & Kudryatsev 2005) and simulated results. All distances are normalized by the bump height $h = 12$mm.

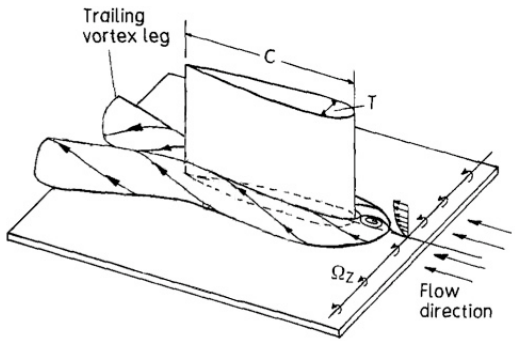

FIGURE 7. Diagram of the flow around a wing-body junction, reproduced from Ryu (2014, Figure 4.1).

ferent quantities of interest are not equally influenced by the wall-blocking. Though this case incorporated more physical complexity, it is still considered a unit level flow relative to most engineering applications. In the next case we investigate a complex 3D flow which is more representative of the complex flows of interest to industry.

3.3. *Wing-body junction*

Corner flows around wall-mounted airfoils are encountered in a variety of industrial applications, the most recognizable being wing-fuselage junctions in aircraft or blade-hub junctions within jet engines. As the flow encounters the wall-mounted objects it is subject to a strong adverse pressure gradient, and complex three-dimensional turbulent structures are formed. In this case we investigate the flow around a symmetric airfoil mounted on a flat plate, first studied experimentally by Devenport & Simpson (1990). This geometry, shown in Figure 7, is dominated by a large horseshoe vortex (HSV) which originates at the leading edge of the wing and wraps around the sides. Additionally, there are several separated flow regions, the two largest of which are upstream of the wing leading edge and at the tail of the wing. Accurate representation of these phenomena is important in predicting the aerodynamic forces or the wall heat transfer.

In this brief we restrict our discussion to demonstrations of the influence of the wall-blocking. Quantitatively we look at profiles of mean streamwise velocity from seven stations upstream of the wing leading edge, as well as contours of R_{13} in the symmetry plane in the same region. The interaction of the incoming boundary layer and the wing

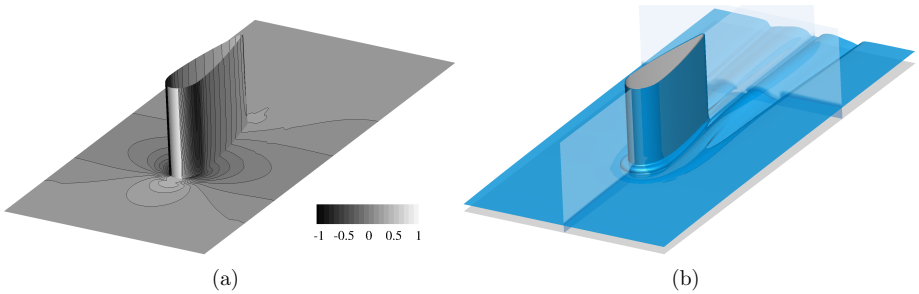

FIGURE 8. Contours of (a) C_p and (b) an isosurface of $F_1 = 0.99$ for the wing body junction, computed using the baseline model.

creates a vortex oriented in the spanwise direction, which then wraps around the airfoil due to convection.

In Figure 8 we show C_P contours along the solid surfaces (wing and flat plate) where the flow moves parallel to the airfoil chord at an angle-of-attack of zero degrees. The second image show an isosurface of the marker $F_1 = 0.99$, as well as contours of F_1 for the symmetry plane (along the airfoil chord) and one plane downstream of the wing. The isosurface show that the near-wall region along the flat plate is much thicker than along the airfoil. For most of the domain the isosurface is planar, but it is influenced by the presence of the horseshoe vortex, which results in several trough-like structures which travel downstream. The region between the $F_1 = 0.99$ isosurface and the solid walls is where the wall-blocking is active.

In Figure 9 we see that the wall-blocking is introducing a modified prediction of the mean velocity profile, in particular for the three measurement stations furthest away from the wing leading edge. For these stations the baseline overpredicts the size of recirculation, e.g., the mean velocity is more negative than that observed in experiments. The leftmost (seventh) station of the experiment shows the velocity profile is all positive (no recirculation), whereas the baseline here still predicts large negative velocity. By introducing anisotropic wall-blocking the prediction for stations 5-7 are improved, and for large Δ_B the upstream recirculation can be reduced significantly (shorter even than the experimental results).

The influence of the wall-blocking is almost negligible for the three stations closest to the wing; the little deviation (relative to the baseline) that does exist is an improvement over the baseline prediction. It appears that the marker F_1 adequately marks the near-wall region; however, to better reproduce the experimental results a different marker should be designed to penetrate further away from the wall. Another observation is that in most of these results a $\Delta_B \leq 0.50$ is appropriate, whereas anything larger tends to overcompensate. This is not surprising, since forcing the entire near-wall region to be perfectly two-component is an unreasonable imposition on the flow. Interestingly, we again observe a trend that the influence of the wall-blocking is asymptotic as Δ_B increases.

The influence on the vortex formed upstream of the leading edge is more visible in Figure 10, which shows contours of R_{13} (the in-plane shear stress at the symmetry plane). By introducing the anisotropic wall-blocking, the vortex location moves closer towards the experimental location and the magnitude of the shear stress increases towards the experimental value. We are only showing DI:TAP results for $\Delta_B = 0.50$ to better illustrate the influence on the upstream vortex formation.

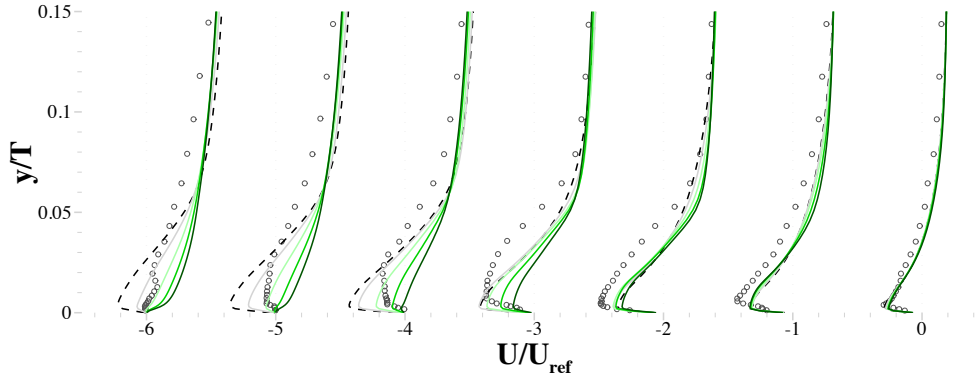

FIGURE 9. Profiles of normalized streamwise velocity from seven stations upstream of the wing leading edge (which would be to the right of the figure). These locations correspond to the first seven experimental measurement stations of Devenport & Simpson (1990), located at $x/T = \{-0.05, -0.10, -0.15, -0.20, -0.25, -0.30, -0.35\}$, respectively. The DI:TAP results are shown by solid lines; darker shades indicate increasing $\Delta_B = \{0.25, 0.50, 0.75, 1.00\}$. The baseline (dashed black line) and experimental results (circles) are provided for reference.

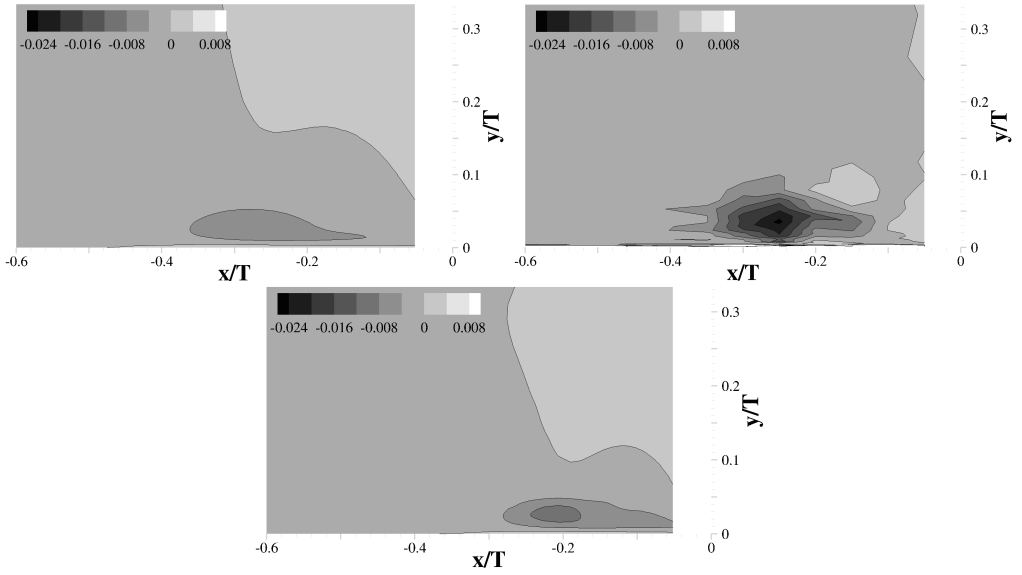

FIGURE 10. Contours of $\overline{u'w'}$ in the symmetry plane upstream of the wing leading edge. Results from the experiment of Devenport & Simpson (1990) (top right), the baseline (top left), and DI:TAP with $\Delta_B = 0.50$ (bottom) are compared.

We examine the qualitative influence on the dynamics of the horseshoe vortex and size of the separated flow regions in the left and right columns of Figure 11, respectively. We compare only the baseline solution and DI:TAP results where $\Delta_B = 1.00$ to highlight the influence of the wall-blocking; however, the same trends are observed for smaller magnitudes of Δ_B. Looking first at contours of strain magnitude, which illustrates locations with high vorticity, we see that the HSV is drawn much closer to the surface of the wing. The DI:TAP HSV shape correlates very well with the shape produced by large-eddy simulation of this flow (Ryu 2014, Figure 4.5). The stand-off distance relative to the leading

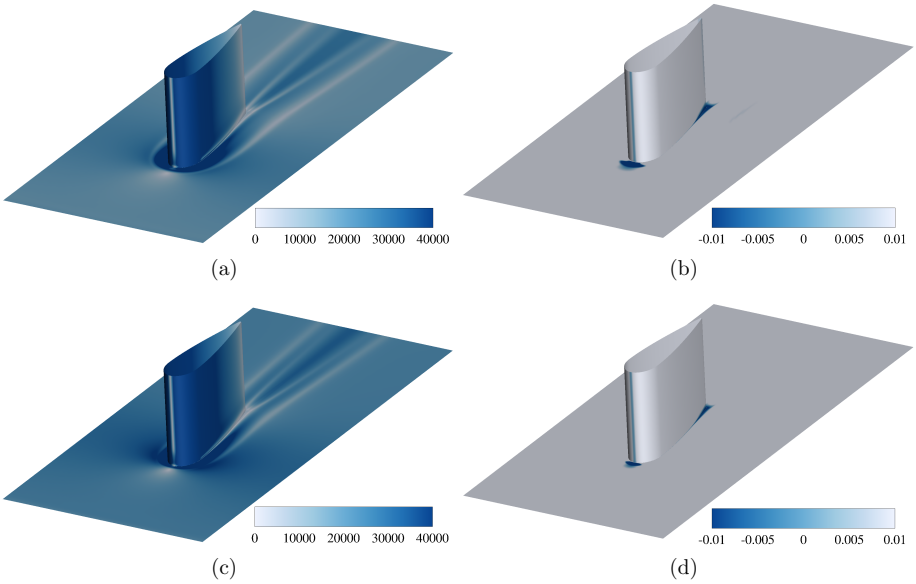

FIGURE 11. Contours of strain magnitude (left column) and negative streamwise velocity (right column) for the wing body junction flow. The results in (a) and (b) are obtained using the baseline model, while (c) and (d) are obtained using the DI:TAP with $\Delta_B = 1.00$.

edge is much shorter, resulting in less spanwise penetration. This discrepancy impacts the wake and flow structures downstream of the wing-body junction, of particular relevance in jet engines where there are successive cascades of turbine or compressor blades. The influence can also be visualized in terms of separated flow regions, depicted by negative streamwise velocity along the walls. Both the stagnation point and wing-tail separated flow regions are reduced in size by the introduction of wall-blocking, a similar result to that observed in the Délery bump.

Though much of the discussion about the wing-body junction has been qualitative, this case has demonstrated again that the anisotropic wall-blocking can improve the performance of the baseline model. It has also demonstrated F_1 as a reasonable marker even in complex flows. Ongoing work involves a more quantitative understanding of how and why introducing anisotropy in these regions is improving the predictive capabilities.

4. Conclusion and future work

We have motivated and implemented a wall-blocking framework for RANS turbulence models based on introducing two-component anisotropic behavior in the near-wall region. Specifically, the turbulence anisotropy eigenvalues are modified such that within the barycentric map they correspond to a location closer to the bottom boundary (the two-component limit). Using the common SST model as the baseline, results were demonstrated for a developed turbulent channel, a transonic separated flow, and the flow around a wing-body junction. For each of these cases, the solution's sensitivity to the strength of the wall-blocking, i.e., the parameter Δ_B, was discussed.

While the approach showed no improvement in the channel, a case in which the SST model is well calibrated, it showed promising results in both the Délery bump and wing-body junction. Of note is that improvement was observed for a baseline which already

has a near-wall correction, i.e., using the $k-\omega$ model. By correlating the anisotropy perturbations to F_1, the blending term which activates $k-\omega$ near walls, our approach produces an SST-like formulation using a different near-wall turbulence model.

The proposed wall-blocking implementation is not unique to the SST, it can be used with any RANS model as the baseline. One of the challenges associated with using a different baseline RANS model is to define an appropriate marker. With the SST we showed that F_1 was not a perfect marker. Ongoing work includes defining a generalized marker which can be used in conjunction with an arbitrary RANS model. Though no additional marker formulations were tested in the present work, there is ongoing research in the use of markers to indicate regions where RANS models are potentially inaccurate (Gorlé *et al.* 2014).

We discussed results using a large range of Δ_B, but only for computations with one baseline model and one direction of perturbation within the barycentric map. It is likely that the optimal value of Δ_B is correlated to the choice of baseline model as well as the direction of perturbation; uncovering this correlation motivates two primary paths of further work. The first is applying the DI:TAP model to additional flows. This effort not only demonstrates the applicability of componentality-based wall-blocking but may provide guidance regarding calibration of Δ_B. The second path is to determine whether moving towards the two-component limit (straight down) in the barycentric map is the best approach. We can easily define alternative directions or trajectories within the barycentric map, potentially discovering an optimal method of introducing anisotropy. Additional work includes evaluating different markers and exploring the solution's robustness relative to the smoothness of the marker.

Acknowledgements

This work was supported by the Department of Energy National Nuclear Security Administration under Award Number DE-NA0002373-1. Additional resources were made available through NSF "MRI-R2: Acquisition of a Hybrid CPU/GPU and Visualization Cluster for Multidisciplinary Studies in Transport Physics with Uncertainty Quantification" support of the Certainty cluster at CTR. The authors would like to thank Rene Pečnik, Alejandro Campos, and Sungmin Ryu for their help setting up and sharing their knowledge of the Délery and wing-body junction test cases, respectively.

REFERENCES

Banerjee, S., Krahl, R., Durst, F. & Zenger, C. 2007 Presentation of anisotropy properties of turbulence, invariants versus eigenvalue approaches. *J. Turbul.* **8**, 1–27.

Billard, F. 2007 *Near-wall turbulence RANS modeling and its applications to industrial cases.* M.Sc. Thesis, University of Manchester.

Délery, J. 1981 Investigation of strong shock turbulent boundary layer interaction in 2D transonic flows with emphasis on turbulence phenomena. In 14^{th} *AIAA Fluid and Plasma Dynamics Conference*.

Devenport, W. & Simpson, R. 1990 Time-dependent and time-averaged turbulence structure near the nose of a wing-body junction. *J. Fluid Mech.* **210**, 23–55.

Durbin, P. 1991 Near-wall turbulence closure modeling without damping functions. *Theor. Comp. Fluid Dyn.* **3**, 1–13.

Durbin, P. 1993 Reynolds-stress model for near-wall turbulence. *J. Fluid Mech.* **249**, 465–498.

Emory, M., Larsson, J. & Iaccarino, G. 2013 Modeling of structural uncertainties in Reynolds-averaged Navier-Stokes closures. *Phys. Fluids* **25**, 110822.

Emory, M. A. 2014 *Estimating model-form uncertainty in Reynolds-averaged Navier-Stokes closures.* PhD Thesis, Stanford University.

Gorlé, C., Larsson, J., Emory, M. & Iaccarino, G. 2014 The deviation from parallel shear flow as an indicator of linear eddy-viscosity model inaccuracy. *Phys. Fluids* **26**, 051702.

Hadjadj, A. & Kudryatsev, A. 2005 Computation and flow visualization in high-speed aerodynamics. *J. Turbul.* **6**, 1–25.

Hoyas, S. & Jimenez, J. 2006 Scaling of the velocity fluctuations in turbulent channels up to $Re_\tau = 2003$. *Phys. Fluids* **18**, 011702.

Kim, J., Moin, P. & Moser, R. 1987 Turbulence statistics in fully developed channel flow at low Reynolds number. *J. Fluid Mech.* **177**, 133–166.

Lien, F. & Kalitzin, G. 2001 Computations of transonic flow with the v^2-f turbulence model. *Int. J. Heat Fluid Fl.* **22**, 53–61.

Loyau, H., Batten, P. & Leschziner, M. 1998 Modeling shock/boundary-layer interaction with nonlinear eddy-viscosity closures. *Flow, Turbul. Combust.* **60**, 257–282.

Manceau, R. & Hanjalić, K. 2002 Elliptic blending model: A new near-wall Reynolds-stress turbulence closure. *Phys. Fluids* **14**, 744–754.

Menter, F. R. 1994 Two-equation eddy-viscosity turbulence models for engineering applications. *AIAA J.* **32**, 1598–1605.

Moin, P. & Kim, J. 1982 Numerical investigation of turbulent channel flow. *J. Fluid Mech.* **118**, 341–377.

Moser, R., Kim, J. & Mansour, N. 1999 Direct numerical simulation of turbulent channel flow up to Re_τ=590. *Phys. Fluids* **11**, 943–945.

O'Sullivan, J., Pečnik, R. & Iaccarino, G. 2012 Capturing near wall effects when applying the Algebraic Structured Based Model. *Proceedings of the Summer Program*, Center for Turbulence Research, Stanford University, pp. 293–302.

Pečnik, R., Terrapon, V. E., Ham, F., Iaccarino, G. & Pitsch, H. 2012 Reynolds-averaged Navier-Stokes simulations of the HyShot II scramjet. *AIAA J.* **50**, 1717–1732.

Ryu, S. 2014 *Large-eddy simulation of a body-junction flow.* PhD Thesis, Stanford University.